ACS APPLIED MATERIALS & INTERFACES

www.acsami.org

Research Article

Magnetic Field-Assisted Stereolithography for Productions of Multimaterial Hierarchical Surface Structures

Erina Baynojir Joyee, Adam Szmelter, David Eddington, and Yayue Pan*

Cite This: *ACS Appl. Mater. Interfaces* 2020, 12, 42357−42368

Read Online

ACCESS | Metrics & More | Article Recommendations

ABSTRACT: Natural organisms provide inspirations for various functional structures and surfaces with significant applications in multidisciplinary fields. These biological systems are generally composed of multiscale surface structures with high geometric complexity and a variety of materials, making it challenging to replicate their characteristics in engineering. This study presents a novel multiscale multimaterial 3D printing method, magnetic field-assisted stereolithography (M-SL), for fabricating hierarchical particle−polymer structures with surface features ranging from a few nanometers to millimeters or even centimeters. Taking inspiration from nature, this study describes the design and fabrication of a bioinspired multiscale hierarchical surface structure, which is characterized of microscale cones, nanoscale pores, and surface wrinkles at a few nanometers. To understand the fundamental physics underlying the hierarchical surface structure fabrication in the proposed M-SL process, the complexities among the M-SL process parameters, material parameters, and printed geometries are discussed. The accuracy of the developed printing method is investigated by comparing the printed geometries and digital designs. Effects of the printed hierarchical surface structure on hydrophobicity and cell viability were characterized and discussed. It was found that the highly hierarchical surface structure changed the polymer composite surface from hydrophilic (contact angle: ∼38°) to hydrophobic (∼146°). In addition, the hierarchical surface structure also created a better environment for cell attachment and growth, with 900% more living cells at 72 h after cell seeding, compared with cells on the nonstructured smooth surface. Local and selective cell seeding can also be enabled by the surface structure design. Experimental results validated the effectiveness of the M-SL 3D printing method on fabricating multimaterial functional objects with hierarchically structured surfaces for a wide spectrum of applications.

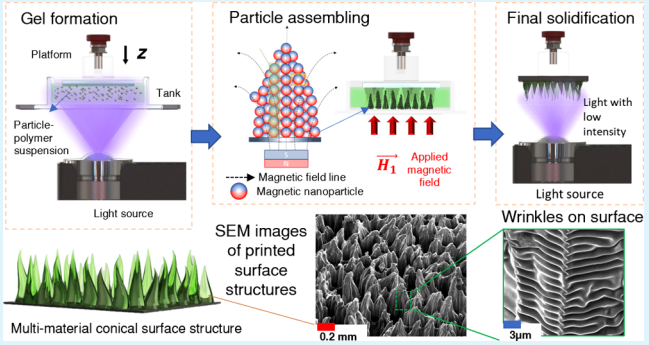

KEYWORDS: *bioinspired structure, multimaterial 3D printing, multiscale manufacturing, surface structuring, stereolithography, wettability, cell attachment and proliferation*

1. INTRODUCTION

Multiscale hierarchical surface structures exhibit enhanced mechanical, optical, hydro, and biological properties in a wide variety of biological organisms.[1−4] In addition, nature demonstrates a wide array of such hierarchical structures composed of soft and hard materials, which are arranged in complex architectures. These structures facilitate multifunctionality such as superhydrophobicity of a rose petal,[5] self-cleaning of a lotus leaf,[6] and oil separation and drag reduction of a Salvinia paradox.[5,7,8] Numerous animals also have good examples of different hierarchical surface structures that exhibit enhanced impact strength[9,10] and dynamic functionalities; for example, the wrinkled cone-like structures in the red mites (*Dermanyssus gallinae*) significantly enhance the friction and adhesion.[11] Other examples include superomniphobic surfaces in Springtails,[12] anti-fogging compound eyes in mosquitos,[13] drag reduction of shark skin,[14] and dry adhesion of gecko foot.[15]

3D hierarchical structures observed in nature that exhibit inherent multifunctional integrations have the following characteristics that are found to be common and often recurring (Figure 1a): (i) the hierarchical surfaces comprise multiscale features (nano- to meso-level); (ii) the multiscale features usually include conical geometry; and (iii) most of the hierarchical structure surfaces are rough, more likely wrinkled and have porous texture. Replication of such hierarchical

Received: June 28, 2020
Accepted: August 20, 2020
Published: August 20, 2020

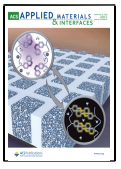

https://dx.doi.org/10.1021/acsami.0c11693
ACS Appl. Mater. Interfaces 2020, 12, 42357−42368

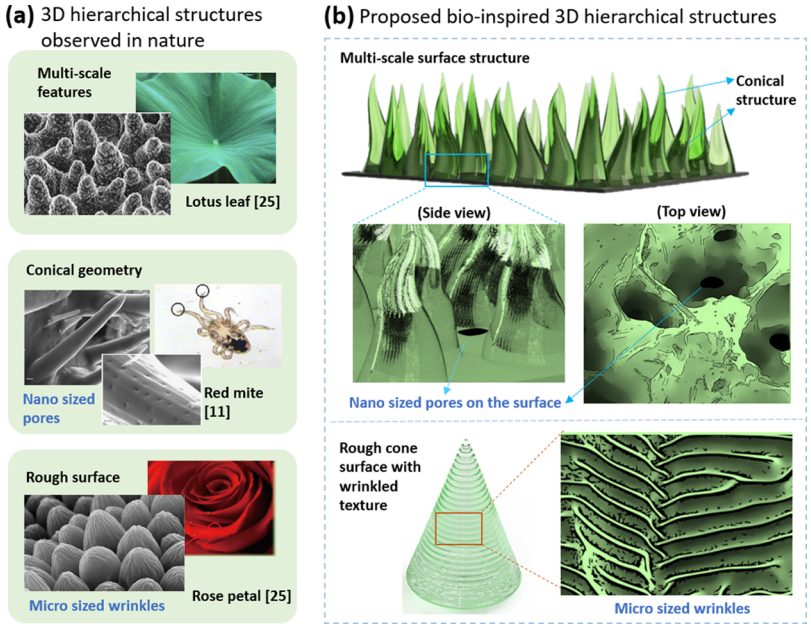

Figure 1. (a) 3D hierarchical functional structures in nature which are characterized by nano- to microscale features, conical geometry, nanosized pores, and microsized surface wrinkles (modified and reprinted from refs 11 and 25); (b) proposed design of replication of such hierarchical structures with cone geometry, porous, and wrinkled surfaces.

structures with conical geometry, wrinkled, and porous surfaces, as shown in Figure 1b, may have a huge potential in diverse real-life applications such as optics, biomedical and material science, mechanics, sensors, and electronics. This creates a demand for multiscale fabrication techniques that can manufacture such complex 3D hierarchical surface structures. However, most traditional fabrication techniques to mimic natural hierarchy have challenges including limited flexibility in structure symmetry and experimental complexity.[1,16] Most of the existing manufacturing techniques are also limited to simple geometry, single scale, and material,[17] which significantly limit upscaling to macroscopic areas and structuring 3D surfaces. It is still quite challenging or even impossible to use conventional fabrication methods to manipulate materials at multiple scales and fabricate complex 3D hierarchical surface structures. In contrast, additive manufacturing (AM) provides an advanced technology platform, capable of fabricating complex 3D objects through layer-by-layer deposition of composite materials. AM technology, therefore, provides a potential solution to fabricate hierarchical multiscale structures.

Several research studies have been conducted to demonstrate AM processes for fabricating multiscale functional structures. These AM processes include fused deposition modeling,[18,19] stereolithography (SL),[20] and inkjet printing.[21] Instead of monolithic process, multiscale structures with different materials have also been developed by integrating different 3D printing processes.[22−24] Li and Chen[25] demonstrated an immersed surface accumulation process (ISAP) to fabricate multiscale multispine array structures inspired by natural cactus, that is capable of highly efficient fog collection. This ISAP method is capable of fabricating micro- to macroscale high-resolution features on existing objects. The two-photon polymerization (TPP) process is another unique process capable of fabricating high-resolution complex 3D microstructures (∼100 nm) without any topological constrains. However, TPP is limited to only transparent resin, has limited depth, and also requires a lot of time to fabricate patterned microfeatures in macroscopic areas and hence is not scalable. Chanda et al.[26] also demonstrated the fabrication of multiscale metamaterials to mimic structured columns of butterfly wings, using a transfer printing method that consists of multiple fabrication processes such as nanoscale transfer printing and laser-based SL material deposition. Despite advances in AM technology, challenges still remain in printing complex geometries with multiscale hierarchical structures. The ranges of the manufacturing scale in the existing manufacturing processes are not comparable to the ones found in nature.[1] Moreover, no manufacturing process can manipulate the material composition at multiple scales without compromising the resolution and building time.

As a potential solution, SL process is an AM technology that has been widely used for various applications that require high precision and fast fabrication.[27] Especially, magnetic field-assisted SL (M-SL) has been validated for fabricating multimaterial structures with pure polymer and particle−polymer composites.[28−30] The particle filling weight ratio could be locally controlled to produce multimaterial objects or heterogeneous composite materials with spatially varied material compositions and hence locally programmed material intelligence and engineered mechanical and magnetic properties. In the literature, a magnetic field-guided 3D printing process has been demonstrated by Erb et al.[31] to fabricate bioinspired complex reinforcement architectures composed of magnetic microplatelets and polymer. Martin et al.[32] used the magnetic field to manipulate material orientation and printed particle−polymer composites. Credi et al.[33] fabricated a composite material via magnetic SL by mixing different concentrations of magnetite particles in the polymer resin. By evaluating the effect of magnetite concentration, they show that it can be an effective approach to produce cheaper microelectromechanical systems devices. Lu et al.[34] used a magnetic field-assisted projection SL process to fabricate magnetic field-responsive smart structures, whereas Safaee and

https://dx.doi.org/10.1021/acsami.0c11693
ACS Appl. Mater. Interfaces 2020, 12, 42357−42368

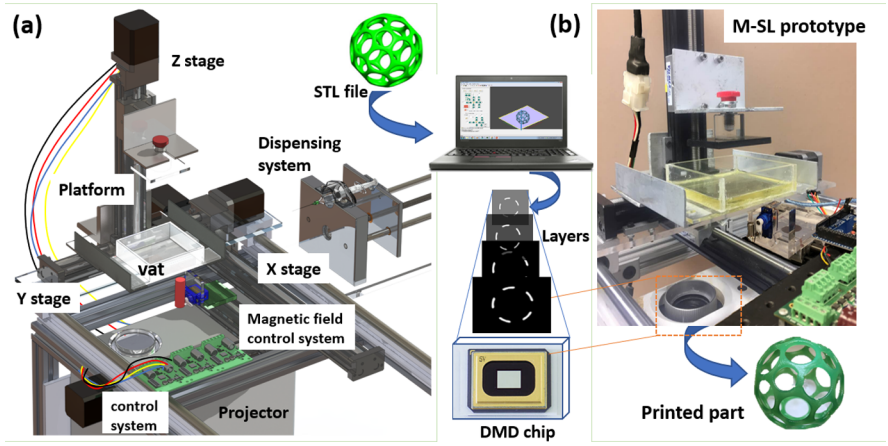

Figure 2. (a) M-SL machine design; (b) M-SL prototype.

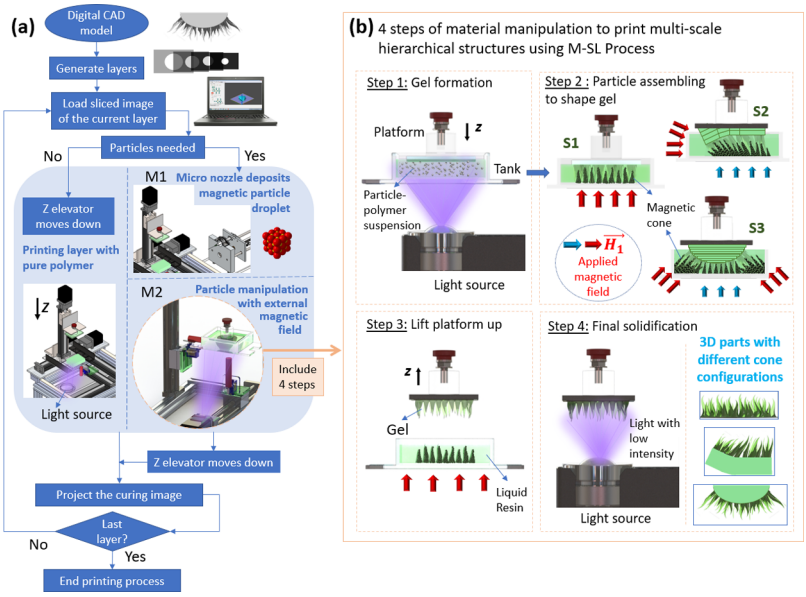

Figure 3. (a) Proposed M-SL process for fabricating multiscale multimaterial wrinkled hierarchical structures; (b) steps for printing the hierarchical surface structures in the M-SL process.

Chen[29] developed an SL process which is able to control the distribution of the magnetic particles (MPs) in functionally graded structures. Joyee and Pan[35,36] further utilized a magnetic field-assisted SL process to fabricate multifunctional soft robots capable of multimodal locomotion in dynamic surfaces.

All the existing studies that employed the magnetic field-assisted SL process primarily focused on multimaterial AM to achieve material intelligence and engineered properties. No work has yet explored the feasibility of manufacturing multiscale hierarchical structures together with multimaterial composition. This study is the first investigation that explored and demonstrated the feasibility of fabricating multiscale (a few nanometers to millimeters or centimeters) hierarchical surface structures with spatially varied material compositions. In this study, a novel M-SL process is developed to fabricate a bioinspired multiscale hierarchical surface structure, which is characterized by cone microstructures with nanowrinkles and nanopores. Complexities among factors such as process parameters, material properties, and model design parameters are analyzed for achieving high-resolution fabrication. Experimental results validated the effectiveness of the M-SL 3D printing method in fabricating functional objects with hierarchically structured surfaces. Although this manufacturing process is enabled to fabricate only conical shape hierarchical structures, driven by the discoveries based on the functional biological structures and the recent material advances, the multimaterial multiscale 3D printing process developed in this study has the potential of enabling future applications in different fields such as biomedical applications, optics, mechanics, microfluidics, soft robotics, and so forth.

2. METHODS AND MATERIALS

2.1. M-SL Experimental Setup. In this study, an M-SL prototype setup was developed.[28] It uses a digital micromirror device (DMD)-based projector as an imaging unit for photocuring. The DMD chip is a microelectro-optical component that enables simultaneous control of ~1×10^6 micromirrors that turn on or off at over 5 kHz. To enable high-resolution image projection, the illumination intensity is adjustable for each micromirror. Digital mask images are created for the sliced 2D layers of the 3D computer aided design (CAD) model. These digital mask images are used as input to the DMD projector. In the M-SL system as shown in Figure 2a, an automated system

https://dx.doi.org/10.1021/acsami.0c11693
ACS Appl. Mater. Interfaces 2020, 12, 42357−42368

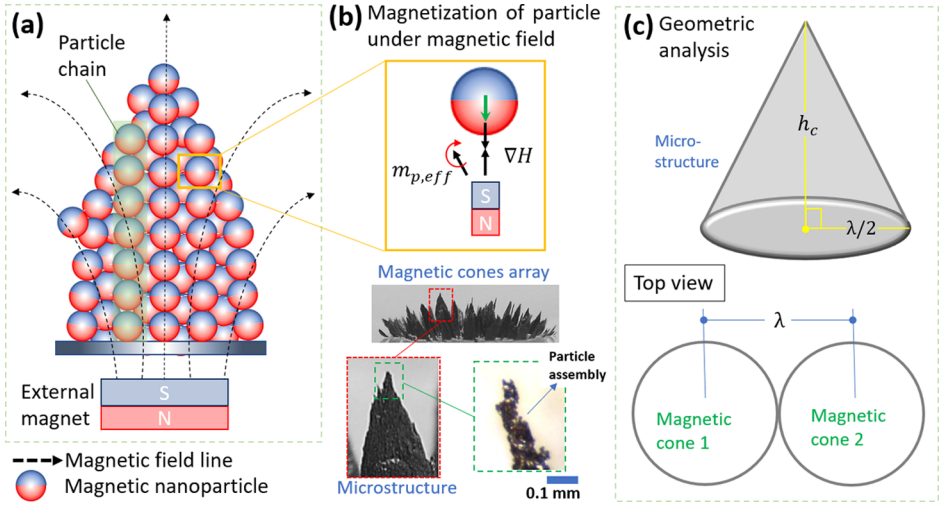

Figure 4. (a) MPs accumulate according to the presence of magnetic field; (b) with the application of the magnetic field, a strong interdipole end-to-end interaction among MPs enables self-assembly into vertical and parallel stacking, which forms 3D microstructures on the substrate; (c) geometrical schematic of the magnetic microstructure as a cone shape.

processes the conversion of CAD model to sliced layers and two sets of digital mask images, the particle deposition image set, and the curing image set. The particle deposition images contain all information required for filling the MPs in the polymer resin, whereas the curing images define the light exposure area to cure the 2D layer.

In this process, MPs or particle suspensions are deposited into the resin vat using a programmable dispensing system. The computerized dispensing system precisely controls the deposited MP volume, while an external magnetic field is used to form the particle filling patterns and ratios. Fast build speed, heterogeneous properties, and localized magnetic characteristics could be achieved.[28,37] After each layer deposition, the DMD-based imaging unit cures particles in desired locations after removing any unwanted particles. After the layer of liquid resin is solidified by the curing image, an automated stage moves up along the *z*-axis to refill the liquid for the next layer curing. A 3D polymer composite or multimaterial part is printed by repeating this process and stacking 2D layers with controlled MPs filling. A prototype of the proposed M-SL process is shown in Figure 2b.

2.2. Multimaterial Multiscale Surface Structure Printing in M-SL. The flowchart in Figure 3a illustrates the proposed M-SL process for printing multimaterial multiscale surface structures. As described in the previous section, the printing process starts with a digital design model, which contains both structural and material composition information. This information is used to generate the appropriate particle deposition image and curing image for each layer.

The images of the current layer are loaded into the main process control program, which activate the *z* elevator to move the platform up. If the images indicate that the layer requires no particles, the platform moves down with a relatively fast velocity to form a resin layer for curing. On the other hand, if the layer needs particle fillers, the process can continue with two different methods. The first method (M1) is used when the layer consists only of multimaterial composition but no surface structure. In M1, the resin vat is aligned with a magnet and then the desired amount of MPs is deposited into the resin vat through a micronozzle. A dynamic magnetic field is formed by moving the magnet, which attracts the MPs within the resin to the desired areas. Method 2 (M2) is used when hierarchical structures need to be printed on the layer surface. As illustrated in Figure 3b, this subprocess includes four steps: step 1: formation of polymer gel; step 2: particle assembling; step 3: lift platform up; and step 4: final solidification.

As illustrated in Figure 3b, initially in step 1, the MPs are suspended uniformly within the polymer resin. Light is projected to polymerize the resin into a gel-like material, in which the MPs are still able to move freely. In step 2, a nonuniform magnetic field is created and applied from the tank bottom (sample1-S1) or side (S2, S3), which in turn creates a particle assembly gradient within the polymer resin. The particles are rearranged along the magnetic field lines. The shapes and directions of the particle assembly can be controlled by the magnetic field strength and direction. In step 2 in Figure 3b, different color arrows illustrate different strengths of the applied magnetic field, with blue denoting a weaker field while red denoting a stronger field. The strong attraction forces of the iron oxide particles assemble them into microsized spherical clusters. These microclusters in turn grow into micrometer- to millimeter-sized hierarchical structures in the resin, given the adequate time which is usually within seconds. The geometry of the structure is a function of the surface tension, polymer gel viscosity, particle size, gravitational force, and the applied magnetic force. Our efforts on modeling the formed geometry are presented in the following Section 2.3.

During the formation of the hierarchical structures, the microclusters of MPs create swelling and wrinkle shapes on the surface of polymer gel. Additionally, in step 2, during gel shaping, a compressive force is generated, which follows the wrinkle lines created by the microclusters. The wavelength of these wrinkles also depends on the diameter of the particle clusters. After removing the printed structure from the platform (step 3), an external permanent magnet is used to pull out the remaining particles from the swollen polymer surface. This task relieves the stress from the polymer surface and facilitates uniform wrinkle generation along the periphery on the surface. In the final step 4, light is projected on the printed surface to fully solidify the structure. After curing of particles, any unwanted particles are removed using an external magnetic field.

2.3. Mechanics of Polymeric Cone Formation and Conical Geometry Modeling. The colloidal MPs create 3D structures by forming reversible chain under the influence of an external magnetic field.[38,39] Under an external magnetic field, the MPs attract each other by dipolar coupling and change its rheological properties by stacking vertically along the direction of the applied magnetic field.[38] In this study, the formation of conical structures follows this self-assembly phenomenon of MPs.

As shown in Figure 4a, the concentration gradient and inherent vertical and parallel stacking of MPs to form a conical structure are enabled by the magnetic force induced on each MP because of the gradient in the magnetic field. Furthermore, the intraparticle attraction and repulsion forces also play an important role in the formation of the 3D conical structures. In the areas closer to the magnet, the magnetic field is quite strong, which attracts the MPs toward it. As the particles come closer to the field, they become magnets themselves. Each particle attracts end-to-end but repels side-to-side. Because they are close to the magnetic field and are further reinforced by the gravitational force, the attraction force is stronger

https://dx.doi.org/10.1021/acsami.0c11693
ACS Appl. Mater. Interfaces 2020, 12, 42357−42368

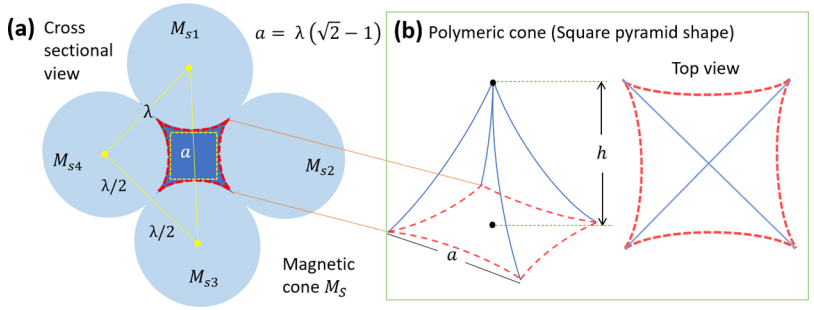

Figure 5. (a) Cross-sectional schematic of polymeric cone formation surrounded by four neighboring magnetic cones; (b) isometric projection and top view of a polymeric cone as a square pyramid.

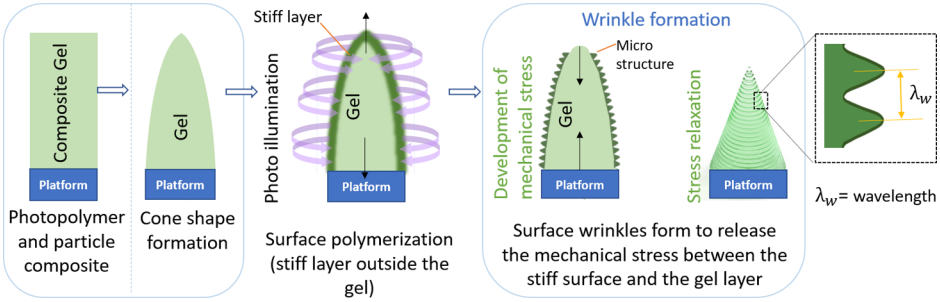

Figure 6. Schematic of wrinkle formation on the surface of polymer composite conical structures.

than the repulsive force. Therefore, they continue stacking and thus form cone-like structures, as shown in Figure 4b.

The structure formation is not only solely governed by the orientation of MPs by the magnetic field but also by the individual magnetophoretic force experienced by the MPs because of the field gradient.[38] This behavior of colloidal MPs under magnetic field should be considered as a complex function of a number of factors including Brownian motion, van der Waals interaction between particles, and magnetic and hydrodynamic forces. The self-assembly of such particles can be predicted by a computational model based on considering the dipole−dipole interaction energy, thermal energy, and the applied magnetic field using[40]

$$h_c = \frac{E_M}{K_B T} \tag{1}$$

where h_c is the length of the particle chain, E_M is the interparticle interaction energy, K_B is the Boltzmann constant, and T is the temperature in kelvin. The interparticle interaction energy can be expressed through the relation of applied magnetic field and particles

$$\partial E_M = \mu_0 \int_0^H m_{P,eff} \cdot dH \cdot \delta V_P \tag{2}$$

here, μ_0 is the magnetic permeability of vacuum and $m_{P,eff}$ is the effective dipole moment acting between particles under an external magnetic field with strength H. If the particles are in a free space then, $m_{P,eff} = MV_P$, where V_P is the volume of a spherical particle with radius r_p and M is the saturation magnetization of the particle. Solving eq 2 for E_m and replacing it in eq 1 leads to

$$h_c = \frac{\mu_0 \pi r_p^3 M^2}{72 K_B T} \tag{3}$$

Because h_c is the total chain length, consisting of multiple MPs with radius r_p stacked on top of each other, the average number of particles per chain n can be predicted by

$$n = \frac{h_c}{2r_p} \tag{4}$$

The magnetic field gradient facilitates magnetophoretic transport, controlled localization, and structural patterning of MPs, creating a concentration gradient ∇n in the base polymer.[38,41] The concentration gradient ∇n for particles in a gradient magnetic field ∇H is given by[38]

$$\nabla n = \frac{n \cdot r_p^3 \pi \mu_0 M \nabla H}{6 K_B T} \tag{5}$$

This concentration gradient will dictate the total volume of the cone (V), as illustrated in Figure 4a. With ∇n concentration gradient in a given cone, the volume can be measured as

$$V = \nabla n \times \text{vol of each nanoparticle sphere}$$

$$V = \nabla n \times \frac{4\pi r_p^3}{3} \tag{6}$$

If the cones are ideally considered to be similar to geometrical cone shapes with height h_c and diameter λ (as shown in Figure 4c), the volume can be computed as

$$V = \frac{\pi \lambda^2 h_c}{12} = \nabla n \times \frac{4\pi r_p^3}{3} \tag{7}$$

From eq 7, the base diameter can be modeled as

$$\lambda = 4\sqrt{\frac{\nabla n r_p^3}{h_c}} \tag{8}$$

In the proposed M-SL process, to fabricate polymeric cone, the primary hypothesis is that when the magnetic cones are formed under the magnetic field, four neighbor magnetic cones shape the polymer gel and create a reverse polymer cone structure, as illustrated in Figure 5a (the cross-sectional schematic diagram). Therefore, for $[n \times n]$ magnetic cones, the number of polymeric cones will be formed is $[(n-1) \times (n-1)]$. As the polymeric cone is formed in the center of the four magnetic cones, the shape of the polymeric cone can be considered as a square pyramid geometry, as shown in Figure 5b.

The diameter (λ) of the magnetic cones can be modeled using eq 8. As illustrated in Figure 5, the base edge of the polymeric square

https://dx.doi.org/10.1021/acsami.0c11693
ACS Appl. Mater. Interfaces 2020, 12, 42357−42368

pyramid a can be measured from the triangle between the centers of three circles (yellow triangle shown in Figure 5a). The resulting shape is an isosceles right triangle, with each leg length being λ. The hypotenuse equals to $\lambda + a = \lambda\sqrt{2}$. Therefore, a can be calculated as

$$a = \lambda(\sqrt{2} - 1) \tag{9}$$

The cone wavelength λ_s can be measured as

$$\lambda_s = a + 2\lambda = a + 8\sqrt{\frac{\nabla n r_p^3}{h_c}} \tag{10}$$

2.4. Mechanics of Surface Wrinkle Formation and Wrinkle Wavelength Modeling. As discussed in the previous section, during the formation of magnetic cones, the MPs form microsphered clusters that create swelling and nonuniform wrinkled shapes on the polymer gel edges. A compressive force is also created at this time. When the conical shaped polymeric gel is subject to an ultraviolet (UV) light source, the light induces photopolymerization at the surface. This forms a stiffer outer polymer layer over a comparatively flexible inner layer of polymer gel. As a result, the gel layer beneath the stiffer polymer layer becomes mechanically unstable and shrinks along the direction, which is normal to the cone surface. This mechanical instability is released through forming a lateral displacement (i.e., wrinkles), off from the center axis along the periphery of the surface,[42] as illustrated in Figure 6.

The elastic instability created by the compressive force and the MP clusters can be defined as buckling, originally formulated by Euler in the 18th century. Figure 6 illustrates the process of wrinkled surface formation because of the inherent mechanical instability. The classical equation for bending of a stiff layer on a more compliant elastic substrate due to mechanical instability can be described as

$$E_c I\frac{d^4 z}{dx^4} + F_c\frac{d^2 z}{dx^2} + ez = 0 \tag{11}$$

where E_c is the Young's modulus of the outer layer, I is the 2nd moment of inertia of the cross section of the cone, e is a coefficient which is a dimension of an elastic modulus of the core material described by Biot,[43] and F_c is the compressive force generated during the formation of the cones in z-axis. The mechanical instability on the polymer surface can be assumed to be similar to a sinusoidal curve with an amplitude of a_w and a wavelength of λ_w, and then the sinusoidal vertical deflection z can be expressed as

$$z(x) = a_w \sin\frac{2\pi x}{\lambda_w} \tag{12}$$

Solving eqs 11 and 12 leads to

$$16E_f I\left(\frac{\pi}{\lambda_w}\right)^4 z - 4F_c\left(\frac{\pi}{\lambda_w}\right)^2 z + ez = 0 \tag{13}$$

$$F_c = 4E_f I\left(\frac{\pi}{\lambda_w}\right)^2 + \frac{k}{4}\left(\frac{\pi}{\lambda_w}\right)^{-2} \tag{14}$$

Differentiating the eq 14 with respect to wavelength will yield a wavelength that can minimize F_c

$$\frac{\partial F_c}{\partial \lambda_w} = 0 = -8E_f I\frac{\pi^2}{\lambda_w^3} + \frac{e\lambda_w}{2\pi^2} \tag{15}$$

According to the hypothesis described in the previous section, the shape of the cone can be considered as a square pyramid geometry. The moment of inertia of the cross section of a square pyramid can be calculated as $I = \frac{1}{36}ah^3$, where h and a are the height and length of base edge of the cone, respectively (Figure 5). Replacing the value of I in eq 15, we can get

$$\lambda_w \approx \pi\left(\frac{E_f a h^3}{k}\right)^{1/4} \tag{16}$$

The length of base a can be measured from eq 9 and the height h of the cone depends on the layer thickness and the light penetration of the photopolymerization process.

Incorporating eqs 5, 8, and 9 into eq 16, the wavelength of the wrinkles can be modeled as

$$\lambda_w = \pi\left(\frac{4(\sqrt{2} - 1)E_f h^3}{k}\right)^{1/4}\left(\frac{n r_p^6 \pi\mu_0 M\nabla H}{6K_B T h_c}\right)^{1/8} \tag{17}$$

2.5. Experimental Characterization. To test the above hypotheses for fabricating multiscale hierarchical surface structures characterized by cone arrays with surface wrinkles, experiments are performed in this study. Two different MPs were tested. EMG 1300 which is a polymer-coated dry magnetic nanoparticle (MNP) of 10 nm diameter from Ferrotec, Inc. and synthetic black magnetic microparticle (MMP) of 0.3 μm diameter in average, purchased from Alpha Chemical (Missouri, USA), were used as the magnetic fillers in experiments.

The properties of these MPs are listed in Table 1. The response of MNPs and MMPs to start the formation of the cone was measured to be around 5 μs in air medium. MMP was chosen because under a nonuniform magnetic field, the MMP's rheological property changes reversibly and instantaneously from a free-flowing particle into a semisolid microstructure by particle stacking. Exposed to a magnetic field, the particles also align in a chain-like fashion with the field direction similar as MNPs. This accumulation of MMP chains restricts the movement of the particles.

Table 1. Properties of Magnetic Particles

	properties		
particles	density at 25 °C g/cm^3	appearance	nominal particle diameter
synthetic black iron-oxide	0.51	black	0.3 μm
EMG 1300 MNPs	1.29	black-brown	10 nm

To mimic the mechanical properties of the conical structures found in nature,[1,8,11] the cones need to be printed using elastic polymers with low Young's modulus so that they are adaptable and can adjust the contact area through mechanical deformation. Furthermore, the printed surface is desired to have engineered flexibility along its body. To engineer such dynamic flexibility in the hierarchical structure, a flexible photocurable polymer Spot-E from SpotA Materials was used as the based polymer in this study.[35] The properties of the flexible resin are summarized in Table 2. From our previous study, it was observed that the rheological and mechanical properties of this elastic polymer composite can be tuned by changing the volume ratio and orientation of the particle fillers.[28]

From the theoretical models in Sections 2.3 and 2.4, it can be observed that the cone structure geometry parameters, that is, the profile and dimension, depend on the M-SL process settings and material parameters. In this study, controllable process parameters include curing time, UV light intensity, and the external magnetic field strength. Curing time and the light wavelength largely affect the curing properties of the polymer resin. They play an important role to shape the proper texture for the polymer gel. The polymer gel texture has to be soft enough to form and adapt shapes but not too soft to flow like a liquid. In the experimental study, the curing time was characterized to be 4−5 s with a 380−420 nm UV light to form the polymer gel. The magnetic field strength is another process parameter that largely affects the MPs and their chain formulation. To identify the proper magnetic field strength for achieving the saturation magnetization of the particle, the external magnetic field was incremented by 685 A/m gradually. With the application of the

https://dx.doi.org/10.1021/acsami.0c11693
ACS Appl. Mater. Interfaces 2020, 12, 42357−42368

Table 2. Properties of Base Polymers

	properties				
polymers	effective light wavelength (nm)	viscosity	mechanical properties	color	density at 25 °C (g/cm^3)
spot E	380−420	∼400 cps	flexible: Young's modulus 12 MPa	light-yellow	1.1

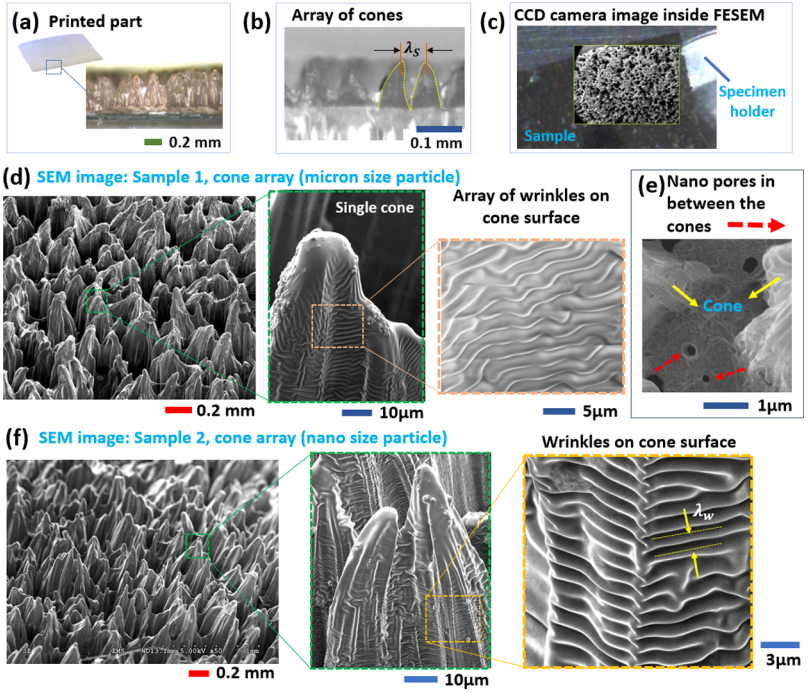

Figure 7. (a) 3D printed part with setae-like hierarchical structures; (b) microscopy image (side view) of the cone array showing the cone wavelength λ_s; (c) CCD camera image inside the electron microscope; (d) SEM images of tilted top view and wrinkles of sample 1; (e) nanosized pores surrounded by cones; (f) SEM images of tilted top view and wrinkles of sample 2.

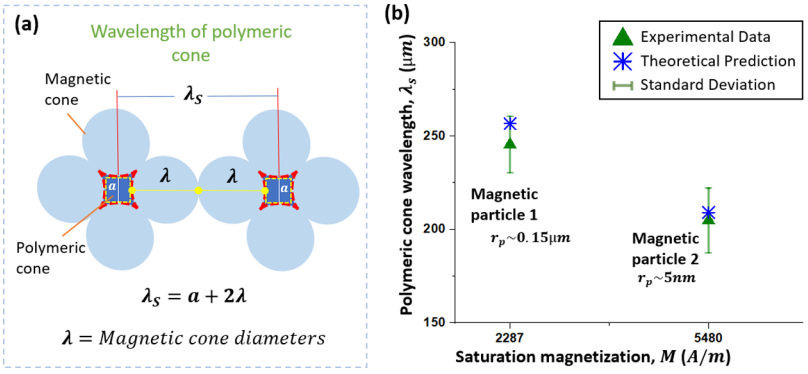

Figure 8. (a) Schematic illustration of polymeric cone formation and related geometry parameters; (b) comparison between theoretical prediction and experimental measurements of cone wavelength λ_s.

external magnetic fields, the MPs align with the direction of the magnetic field, creating a strong magnetic flux density. When the magnetic field strength reaches a certain threshold, the magnetic domain cannot exceed further, and a saturated magnetization is achieved. This saturation magnetization was approximated by the applied external magnetic field, which has the lowest strength and forms the magnetic cones. As discussed in the models in previous section, this saturation magnetization affects the overall texture and magneto-mechanical properties of the printed parts. In this study, two different magnetic fields were identified experimentally for reaching the saturation magnetization for two different sizes of MPs.

Material parameters in this study include particle size, polymer viscosity, and particle/resin volume ratio. Two different sized particles of 10 nm and 0.3 μm diameters were used to print samples. Additionally, the density of hierarchical structure formation largely depends on the volume ratio of particles. A high ratio of particle to polymer can block the UV light, which could result in a lower density of the cone array. Polymer viscosity is an important material parameter, as the particle movement is strongly affected by the suspension viscosity. In this study, the polymer resin with a relatively low viscosity (∼400 cps) was investigated experimentally. Based on the input (process and material) parameters, output parameters that describe the printed hierarchical structure geometry such as the cone height, cone wavelength, and surface wrinkle wavelength were measured experimentally to validate the hypotheses and the proposed theoretical models.

https://dx.doi.org/10.1021/acsami.0c11693
ACS Appl. Mater. Interfaces 2020, 12, 42357−42368

3. RESULTS AND DISCUSSION

In our experiment, two sample groups are designed and printed using the M-SL process described in Section 2. Sample group 1 is printed by using iron oxide particle of diameter 0.3 μm and sample group 2 is printed by using the iron oxide particle of diameter 10 nm. Both the printed parts have a size of 10 mm × 10 mm. The microstructures of printed cone arrays are observed from a scanning electron microscope. The scanning electron microscopy (SEM) images are recorded using a JEOL JSM-6320F (CA, USA) electron microscope operated at 5 kV. Figure 7a,b shows a printed part and typical optical microscopy images of the hierarchical structure array on the surface. From the SEM images (Figure 7c–f) of the cone array, individual cone and the wrinkles distributed on the surface of the cones can be observed on both group-1 samples and group-2 samples. On average, the cones are about 100 μm long, with ~2.5 μm deep wrinkles for group-1 samples and 70 μm long with ~1 μm deep wrinkles for group-2 samples. After an external magnetic field was applied to remove all the remaining MPs loosely adhered on the printed part, nano- to microsized holes are left in between the cone bases, as shown in Figure 7e. For both groups of samples, these holes are about 10–20 nm diameters.

3.1. Effects of Manufacturing Process on Printed Geometry. To validate the theoretical models proposed in Section 2 and better understand the printed hierarchical structure, the experimental characterizations of the two printed sample groups were compared with the theoretical predictions calculated using eq 10, as shown in Figure 8. The cone wavelength of the printed composite samples was characterized experimentally using a MicroVu Sol 161 optical microscope (Windsor, CA, US). The experimental cone wavelength (λ_s) was an average value of the peak-to-peak distance among cone tips. Five replicates were done for each experiment. For group-1 samples in which the average diameter of the particle fillers is 0.3 μm, the mean λ_s was found to be 245.40 μm with a standard deviation of 15.11 μm. For the second group of samples in which the average diameter of the particle fillers is 10 nm, the mean λ_s was found to be 204.20 μm with a standard deviation of 17.33 μm. For both particles, the experimental λ_s measurements were smaller compared to their theoretical predictions (256.53 and 209.05 μm, respectively, for group-1 samples and group-2 samples) (Figure 8b). A possible reason can be that the λ_s predicted using eq 10 is dependent on the saturation magnetization, M of the MPs. To determine the λ_s value, the experimentally identified threshold magnetic field strength was used to approximate the value of M. As mentioned previously in Section 2.5, discrete units of Magnet 1 (685 A/m) and Magnet 2 (116 A/m) were incrementally applied to identify the threshold. In addition, the saturation magnetization was approximated to be same as the magnetic field threshold, which is actually larger than the true saturation magnetization value. This causes the prediction to be slightly larger than the experimentally characterized λ_s, which reflects the original saturation magnetization.

A comparison of the experimentally measured surface wrinkle wavelength (λ_w) and the theoretical predictions calculated using eq 17 is also shown in Figure 9. The experimental λ_w was measured as the average wrinkle peak-to-peak distance from the acquired SEM images (shown in Figure 7f). Five replicates were done for each experiment. For group-1 samples, the mean λ_w was 2.50 μm with a standard deviation of 0.58 μm. For group-2 samples, the mean λ_w was 1.01 μm with a standard deviation of 0.48 μm. From the results shown in Figure 9, it can be observed that λ_w increases with the increase of the particle diameter. Also, the experimental λ_w values are slightly smaller compared to the theoretical predictions (2.87 and 1.55 μm, respectively, for group-1 and group-2 samples). This can also be explained by the overlarge saturation magnetization approximation used in predictions as explained previously for λ_s.

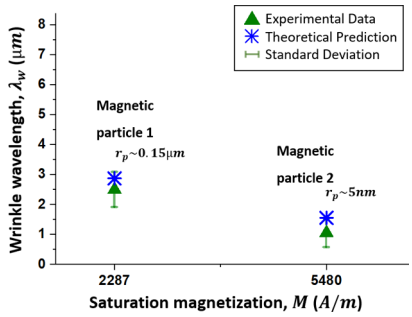

Figure 9. Comparison between theoretical predictions and experimental values of wrinkle wavelength λ_w.

As shown in Figures 8b and 9, the predicted cone wavelength and surface wrinkle wavelength agree well with the experimental measurements. For both wavelengths of the two groups samples, the predictions fall within a standard deviation. The experimental results validated the hypothesized surface structuring mechanics and the prediction models developed in Section 2 with statistical significance.

3.2. Spatially Varied Material Composition of the Surface Structure. The multimaterial surface structures have varying particle–polymer concentrations, allowing dynamic flexibility along the axial direction of the microcones on the surface. The cone top surface is composed of pure polymer resin and hence more flexible compared to the base which is composed of particle–polymer composites. As discussed in Section 2, the amount of MPs in the printed cone depends on the particle distribution during the printing process. As illustrated in Figure 3b, after step 2, the top surface of the cones is at the bottom of the tank, where the magnetic field is the strongest. Under a strong external magnetic field, the MPs assembled together closely at the bottom of the tank to create magnetic cones (Figure 3b), concurrently creating polymer cone top surface in the opposite direction. At this point, the magnetic field at the upper area of the tank is much weaker, which results in more free MPs in the resin. Therefore, at the lower base area of the polymeric cone, a large number of free MPs are cured into the polymer gel during the photopolymerization process. The bottom of the cones is therefore comparatively stiffer and can ensure strength at the base and intracone regions to withstand the external forces. This gradient weight ratio of the magnetic iron oxide particles along top to bottom of the conical structure allows surface rigidity, while easy deformation and good elasticity, which are usually conflicted properties, cannot be possessed by a nonstructured smooth surface.

The material composition and weight ratio can be controlled during the printing process after MP assembling in the base resin. One method is to change the distance between the external magnet and the tank. Larger distance will reduce the magnetic field strength at the tank bottom. Weaker magnetic field will result in weaker particle assembly at the bottom.

https://dx.doi.org/10.1021/acsami.0c11693
ACS Appl. Mater. Interfaces 2020, 12, 42357–42368

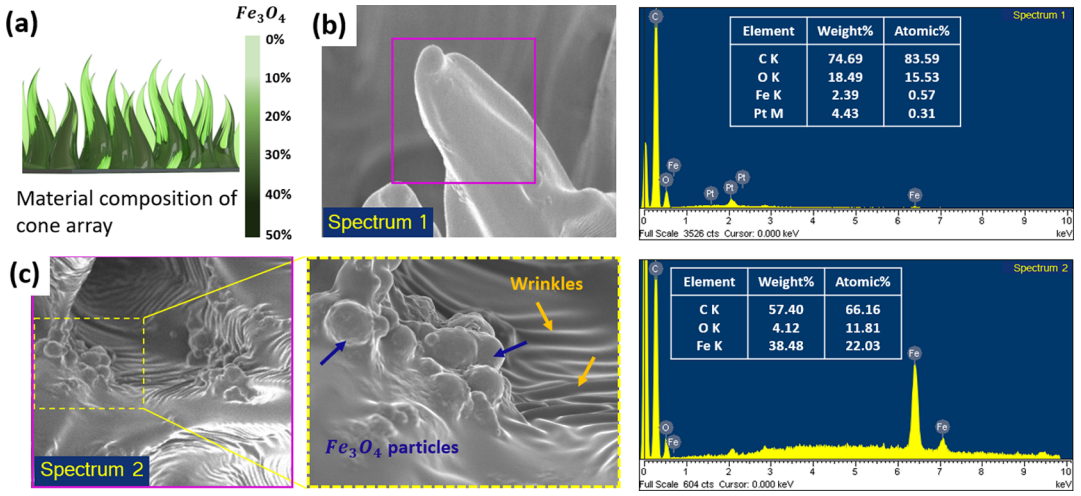

Figure 10. (a) Multimaterial design of the conical surface structure, which is characterized by the gradient distribution of MPs over the cone; (b) SEM image of a single cone and corresponding EDS; and (c) SEM image of the base and intracone region of the cones and corresponding EDS.

Therefore, the iron oxide particle ratio at the cone top surface will be higher with a reduced flexibility. In this case, the mechanical property difference between the cone top surface and base will be smaller. Another way to control the particle weight ratio in the printed part is to control the exposure time of the magnetic field. If the magnetic field is removed before the saturation time, the MP assemblies will be smaller, resulting in more free particles in the base resin. This will change the spatial distribution of MPs and material compositions in the different regions of the conical structures, also changing the mechanical properties of the cone base and top surface.

In this test case, a magnetic field with a strength of 2287 A/m is used on the tank bottom with a distance of 5 mm and an exposure time ranging from 1 to 3 s to print the conical structure with a gradient weight ratio of ~40 wt % of Fe_3O_4 in the cone base to 0 wt % in the cone top surface (Figure 10a). A schematic and SEM images of the printed conical structure with the gradient material composition are shown in Figure 10. The energy-dispersive spectrum (EDS) was also measured in the top surface (Spectrum 1, Figure 10b) and side surfaces (Spectrum 2, Figure 10c) of the cone structure. The analysis shows a major peak of magnetic iron oxide particles in the side surfaces of the cone. At the side surfaces of the cone, the wt % of Fe_3O_4 is 38.48%, compared to 2.39% at the top of the cone. There were an overall 16% more iron oxide particles on the side surface compared to the top surface of the cone. In future, more study will be done to understand the influence of the magnetic field strength and magnetic exposure time on the printed material composition.

3.3. Effects of the Surface Structure on Hydrophobicity. A common example of the hydrophobic property can be found in nature is the rose petals, which have microstructures with cuticular wrinkles or folds. This kind of rough microscopic hierarchical surface generally creates air pockets, which drastically reduce the solid−liquid contact. The reduced solid−liquid contact area allows the water droplet to form almost near-perfect spheres which easily rolls off the surface, making the surface hydrophobic and enabling self-cleaning.[1]

In this study, the wetting property of the printed structured surface samples was tested and compared with nonstructured smooth surface samples, which were printed using the same process settings and composed of the same material compositions. The wetting behavior of a surface is primarily governed by either surface geometrical structure or chemical composition.[44] Theoretically, according to the Young contact angle model for the contact angle[45] and the Cassie model,[46] the introduction of surface hierarchy and increased roughness of such hierarchy prevent complete contact between the water droplet and the nonwetted surface.[44] The Cassie roughness factor was further idealized with a pillar array-based hierarchical architecture by Barbieri et al.;[47] the factor depends proportionally on the number of pillar (cones) per unit area and surface area of the cones, while it depends inversely on total area enclosed by a liquid droplet between two neighbor cones. Specifically, for our proposed surface structure, the tapered shape of the conical structures and wrinkles along their surface increase the surface roughness. Furthermore, the conical structures create a network of nanocavities in between the cones. These cavities along with tapered shape cones retain nano- to microsized air bubbles within the structure, leading to reduced contact area with liquid droplets and hence inducing near-superhydrophobic behaviors from a surface made of naturally hydrophilic polymer. To compare the contact angle between nonstructured smooth surface and surface with hierarchical structures, a micropipette was used to pick up water and place the droplet on the surface. The tip of the micropipette was able to create water droplets of 0.5−10 μL, as shown in Figure 11a. A water droplet on a nonstructured smooth surface is shown in Figure 11b. The water droplet creates an average contact angle of 38° on the smooth surface, demonstrating the hydrophilic nature of the surface. In contrast, the water droplet creates a much higher contact angle (125−146°) with the surface with hierarchical structures, as shown in Figure 11c,d. Both of the printed sample surfaces (group-1 sample and group-2 sample) with hierarchical structures showed hydrophobic properties. The surface−liquid contact angle was measured to be 125° on average for group-1 samples and 146° on average for group-2 samples, as shown in Figure 11c,d, respectively. The experimental results show that the hierarchical surface structure investigated in this study is capable of changing a naturally hydrophilic surface to hydrophobic or even superhydrophobic. This kind of surface will be suitable for a wide array of interface applications, bioapplications, and microfluidics applications.

https://dx.doi.org/10.1021/acsami.0c11693
ACS Appl. Mater. Interfaces 2020, 12, 42357−42368

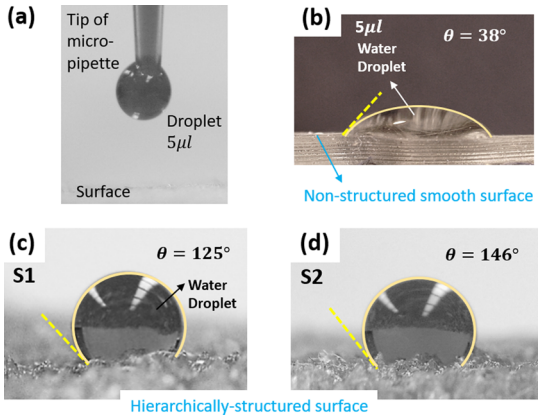

Figure 11. (a) Water droplet and the tip of the micropipette, which is able to create a droplet with a volume of 0.5 to 10 μL; (b) droplet on a nonstructured smooth surface; (c,d) droplet on group-1 sample surfaces and group-2 sample surfaces which comprise hierarchical surface structures; (c) group-1 sample surfaces demonstrating an average contact angle of 125°; (d) group-2 sample surfaces demonstrating an average contact angle of 146°. All samples were printed using the same polymer material.

3.4. Effects of the Surface Structure on Cell Attachment and Growth. Different studies from the literature[48,49] have hypothesized that unique wrinkled hierarchical surface structures like our printed samples not only show hydrophobicity but also have great potential for bio applications because of their inherent biocompatibility with the living cells or tissues. In this study, we tested and validated this hypothesis by seeding some human-umbilical venous endothelial cells on our printed parts (as shown in Figure 12a). We seeded cells on printed parts with smooth surface and with hierarchically structured surfaces. The cells were seeded at a density of around 4000/cm^2 and the passage number was 4. Then, the cells were grown in an incubator with 5% CO_2 at 37 °C temperature. Before imaging the cells, the cell cytoplasm was stained for 30 min in an incubator with Calcein AM. Calcein is able to show the viability of living cells, which can become fluorescent after hydrolysis because of the intracellular enzymes. A confocal microscope from Zeiss (LSM 710) was used to record the images at 6 and 72 h after seeding the cells. 3D image stacks with 317 2D slices were acquired with a step size of 0.77 μm. The green channel of the images highlighted Calcein, whereas the blue channel highlighted material autofluorescence. These images were imported into MATLAB to be analyzed as individual 2D images. A maximum 3D intensity projection image created using the Zeiss ZEN Lite software shows the density of seeded cells on both surfaces. Figure 12c–f shows the 3D reconstruction of the cell distribution on the smooth and wrinkled hierarchical surface. It can be observed that the cell attachment on the structured surface was almost 9 times higher compared to the smooth surface at 72 h after cell seeding. This implies that the hierarchical surface structure is able to provide a comparatively better environment for the seeded cells to attach and grow.

Within the different slices (in Z-axis) of the hierarchical surface, it was observed that the cell density was highest (approx. 38 per mm^2) in the middle slices (Figure 13b, $Z \approx 55$ μm), whereas much lower at the top (approx. 9 per mm^2) (Figure 13a, $Z \approx 155$ μm) and bottom slices (approx. 7 per mm^2) (Figure 13c, $Z \approx 5$ μm). This was due to the large number of endothelial cells on the wrinkled surface and concurrent gaps between the conical structures on the surface. Compared to the cone middle section covered by wrinkle textures, the cone top surface was comparatively smooth, resulting in a lower cell density. For the bottom section of the conical structure, the space is limited, which inhibited the cell attachment. Compared to the cell size of 14–15 μm, the average space among cones on the bottom (where $z \approx 5$ μm) was ~10 μm. The middle section provides adequate growing space for the cells, allowing the cells to live and grow on the wrinkled surface even after 72 h. These results explained how the attachment and growth of living cells can be spatially manipulated through designing hierarchical surface structures. From the literature, we can see that different wrinkled graphene-based surfaces[50] or hydrogel surfaces[51] have been used to control cell alignment, morphology, and differentiation.

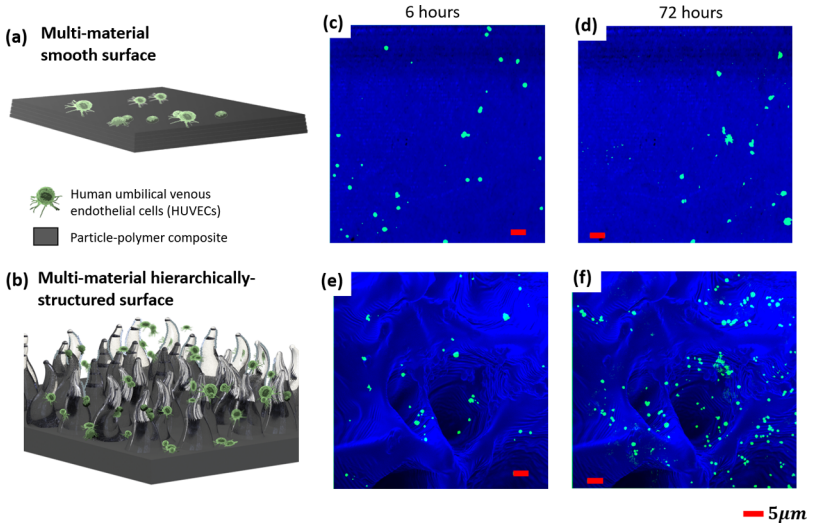

Figure 12. Cell viability of the printed part. (a,b) Schematic of the seeded cells on a multimaterial smooth surface which has no conical structures and a multimaterial surface which is covered by the hierarchical structure. (c–f) 3D reconstructions of the confocal microscopy images of the cells on the printed composite surfaces; smooth surface after 6 (c) and 72 h (d) of seeding; hierarchically structured surface after 6 (e) and 72 h (f) of seeding. Green: living cells; blue: surface.

https://dx.doi.org/10.1021/acsami.0c11693
ACS Appl. Mater. Interfaces 2020, 12, 42357–42368

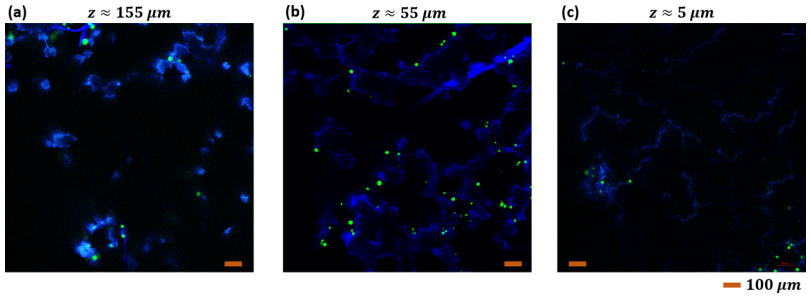

Figure 13. Confocal microscopy images of cells growing over the hierarchical surface at different Z-axes after 72 h of seeding. Image captured at (a) $Z \approx 155$ μm (cone top); (b) $Z \approx 55$ μm (cone middle); (c) $Z \approx 5$ μm (cone bottom). Green: living cells; blue: structured surface.

Because the hierarchical structure was significantly favorable to cell growth, future studies can be conducted to investigate the advantages of the structure for such cell culture applications, using surface geometry and wrinkles to act as scaffolds for controlled cell proliferation.

4. CONCLUSIONS AND FUTURE WORK

In conclusion, a novel M-SL technique has been proposed in this study to fabricate multiscale (nm to μm) hierarchical surface structures with particle−polymer composite material manipulation, inspired by nature. The relationship among material properties, manufacturing process parameters and surface structure geometry parameters have been analyzed and experimentally validated. The mechanics of formation of cone and subsequent cone surface wrinkles in the proposed M-SL process have been described and modeled analytically. Effects of the manufacturing parameters and material properties on printed surface structure geometries, including the printed conical structure height, cone, and wrinkle wavelengths, were analytically modeled and experimentally characterized. The hierarchical surface structures were also tested for wetting properties. Experimental results showed that the hierarchical surface structures changed the polymer composite surface from hydrophilic to hydrophobic, with the solid−liquid contact angle increasing from 38 to 146°. Moreover, the multimaterial multiscale hierarchical surface structure demonstrated superior biocompatibility for enhancing cell attachment and growth (∼9 times more cells), compared to the cell viability results of a nonstructured smooth surface. A high correspondence between the surface structure geometry and the cell amount was also observed. The study validates the effectiveness of M-SL technique for fabricating bioinspired multimaterial multiscale hierarchical surface structures, which can enable several future real-life applications. Future work will focus on investigations of the material composition control during the surface structure printing process using the M-SL method.

AUTHOR INFORMATION

Corresponding Author

Yayue Pan − *Department of Mechanical and Industrial Engineering, University of Illinois at Chicago, Chicago 60607-7042, Illinois, United States;* orcid.org/0000-0003-0797-1697; Phone: +1-312-996-8777; Email: yayuepan@uic.edu

Authors

Erina Baynojir Joyee − *Department of Mechanical and Industrial Engineering, University of Illinois at Chicago, Chicago 60607-7042, Illinois, United States*

Adam Szmelter − *Department of Bioengineering, University of Illinois at Chicago, Chicago 60607-7042, Illinois, United States*

David Eddington − *Department of Bioengineering, University of Illinois at Chicago, Chicago 60607-7042, Illinois, United States*

Complete contact information is available at: https://pubs.acs.org/10.1021/acsami.0c11693

Notes

The authors declare no competing financial interest.

REFERENCES

(1) Yang, Y.; Song, X.; Li, X.; Chen, Z.; Zhou, C.; Zhou, Q.; Chen, Y. Recent Progress in Biomimetic Additive Manufacturing Technology: From Materials to Functional Structures. *Adv. Mater.* **2018**, *30*, 1706539.

(2) Yang, Y.; Chen, Y.; Li, Y.; Chen, M. Z. Q.; Wei, Y. Bioinspired Robotic Fingers Based on Pneumatic Actuator and 3D Printing of Smart Material. *Soft Robot.* **2017**, *4*, 147−162.

(3) Yang, Y.; Chen, Z.; Song, X.; Zhang, Z.; Zhang, J.; Shung, K. K.; Zhou, Q.; Chen, Y. Biomimetic Anisotropic Reinforcement Architectures by Electrically Assisted Nanocomposite 3D Printing. *Adv. Mater.* **2017**, *29*, 1605750.

(4) Hu, W.; Lum, G. Z.; Mastrangeli, M.; Sitti, M. Small-scale Soft-bodied Robot with Multimodal Locomotion. *Nature* **2018**, *554*, 81.

(5) Yang, Y.; Li, X.; Zheng, X.; Chen, Z.; Zhou, Q.; Chen, Y. 3D-Printed Biomimetic Super-Hydrophobic Structure for Microdroplet Manipulation and Oil/Water Separation. *Adv. Mater.* **2018**, *30*, 1704912.

(6) Wang, T.; Chang, L.; Hatton, B.; Kong, J.; Chen, G.; Jia, Y.; Xiong, D.; Wong, C. Preparation and Hydrophobicity of Biomorphic ZnO/carbon Based on a Lotus-leaf Template. *Mater. Sci. Eng., C* **2014**, *43*, 310−316.

(7) Yao, X.; Song, Y.; Jiang, L. Applications of Bio-inspired Special Wettable Surfaces. *Adv. Mater.* **2011**, *23*, 719−734.

(8) Barthlott, W.; Schimmel, T.; Wiersch, S.; Koch, K.; Brede, M.; Barczewski, M.; Walheim, S.; Weis, A.; Kaltenmaier, A.; Leder, A. The Salvinia Paradox: Superhydrophobic Surfaces with Hydrophilic Pins for Air Retention Under Water. *Adv. Mater.* **2010**, *22*, 2325−2328.

(9) Bohn, K.; Jiang, L. Bio-inspired Design of Multiscale Structures for Function Integration. *Nano Today* **2011**, *6*, 155−175.

(10) Saranathan, V.; Osuji, C. O.; Mochrie, S. G. J.; Noh, H.; Narayanan, S.; Sandy, A.; Dufresne, E. R.; Prum, R. O. Structure, Function, and Self-assembly of Single Network Gyroid (I4132) Photonic Crystals in Butterfly Wing Scales. *Proc. Natl. Acad. Sci.* **2010**, *107*, 11676−11681.

(11) Cruz, M. D. S.; Vega Robles, M. C.; Jespersen, J. B.; Kilpinen, O.; Birkett, M.; Dewhirst, S.; Pickett, J. Scanning Electron Microscopy of Foreleg Tarsal Sense Organs of the Poultry Red Mite, Dermanyssus Gallinae (DeGeer)(Acari: Dermanyssidae). *Micron* **2005**, *36*, 415−421.

(12) Yun, G.-T.; Jung, W.-B.; Oh, M. S.; Jang, G. M.; Baek, J.; Kim, N. I.; Im, S. G.; Jung, H.-T. Springtail-inspired Superomniphobic

Surface with Extreme Pressure Resistance. *Sci. Adv.* **2018**, *4*, No. eaat4978.
(13) Gao, X.; Yan, X.; Yao, X.; Xu, L.; Zhang, K.; Zhang, J.; Yang, B.; Jiang, L. The Dry-style Antifogging Properties of Mosquito Compound Eyes and Artificial Analogues Prepared by Soft Lithography. *Adv. Mater.* **2007**, *19*, 2213−2217.
(14) Wen, L.; Weaver, J. C.; Thornycroft, P. J. M.; Lauder, G. V. Hydrodynamic Function of Biomimetic Shark Skin: Effect of Denticle Pattern and Spacing. *Bioinspiration Biomimetics* **2015**, *10*, 066010.
(15) Tian, Y.; Pesika, N.; Zeng, H.; Rosenberg, K.; Zhao, B.; McGuiggan, P.; Autumn, K.; Israelachvili, J. Adhesion and Friction in Gecko Toe Attachment and Detachment. *Proc. Natl. Acad. Sci.* **2006**, *103*, 19320−19325.
(16) Li, X.; Yang, Y.; Chen, Y. Bio-Inspired Micro-Scale Texture Fabrication Based on Immersed Surface Accumulation Process. *Proceeding of 2017 World Congress on Micro and Nano Manufacturing*, 2017; pp 33−36.
(17) Potter, K. D. The Early History of the Resin Transfer Moulding Process for Aerospace Applications. *Composites, Part A* **1999**, *30*, 619−621.
(18) Cook, K.; Canning, J.; Leon-Saval, S.; Reid, Z.; Hossain, M. A.; Comatti, J.-E.; Luo, Y.; Peng, G.-D. Air-structured Optical Fiber Drawn from a 3D-printed Preform. *Opt. Lett.* **2015**, *40*, 3966−3969.
(19) Cox, W. R.; Chen, T.; Hayes, D. J. Micro-optics Fabrication by Ink-jet Printers. *Opt. Photonics News* **2001**, *12*, 32−35.
(20) Wu, D.; Wang, J.-N.; Niu, L.-G.; Zhang, X. L.; Wu, S. Z.; Chen, Q.-D.; Lee, L. P.; Sun, H. B. Bioinspired Fabrication of High-Quality 3D Artificial Compound Eyes by Voxel-Modulation Femtosecond Laser Writing for Distortion-Free Wide-Field-of-View Imaging. *Adv. Opt. Mater.* **2014**, *2*, 751−758.
(21) Bai, L.; Xie, Z.; Wang, W.; Yuan, C.; Zhao, Y.; Mu, Z.; Zhong, Q.; Gu, Z. Bio-inspired Vapor-responsive Colloidal Photonic Crystal Patterns by Inkjet Printing. *ACS Nano* **2014**, *8*, 11094−11100.
(22) Li, X.; Baldacchin, T.; Song, X.; Chen, Y. Multi-scale Additive Manufacturing: An Investigation on Building Objects with Macro-, Micro-and Nano-scales Features. *11th International Conference on Micro Manufacturing*, 2016.
(23) Choi, J.-W.; Yamashita, M.; Sakakibara, J.; Kaji, Y.; Oshika, T.; Wicker, R. B. Combined Micro and Macro Additive Manufacturing of a Swirling Flow Coaxial Phacoemulsifier Sleeve with Internal Micro-vanes. *Biomed. Microdevices* **2010**, *12*, 875−886.
(24) Hengsbach, S.; Lantada, A. D. Rapid Prototyping of Multi-scale Biomedical Microdevices by Combining Additive Manufacturing Technologies. *Biomed. Microdevices* **2014**, *16*, 617−627.
(25) Li, X.; Chen, Y. Multi-scale 3D Printing of Bioinspired Structures with Functional Surfaces. *2018 International Symposium on Flexible Automation*, 2018; pp 13−20.
(26) Chanda, D.; Shigeta, K.; Gupta, S.; Cain, T.; Carlson, A.; Mihi, A.; Baca, A. J.; Bogart, G. R.; Braun, P.; Rogers, J. A. Large-area Flexible 3D Optical Negative Index Metamaterial Formed by Nanotransfer Printing. *Nat. Nanotechnol.* **2011**, *6*, 402−407.
(27) Lu, L.; Joyee, E. B.; Pan, Y. Correlation Between Microscale Magnetic Particle Distribution and Magnetic-Field-Responsive Performance of Three-Dimensional Printed Composites. *J. Micro Nano-Manuf.* **2018**, *6*, 010904.
(28) Joyee, E. B.; Lu, L.; Pan, Y. Analysis of Mechanical Behavior of 3D Printed Heterogeneous Particle-polymer composites. *Composites, Part B* **2019**, *173*, 106840.
(29) Safaee, S.; Chen, R. Investigation of a Magnetic Field-Assisted Digital-Light-Processing Stereolithography for Functionally Graded Materials. *Procedia Manuf* **2019**, *34*, 731−737.
(30) Nagarajan, B.; Eufracio Aguilera, A. F.; Wiechmann, M.; Qureshi, A. J.; Mertiny, P. Characterization of Magnetic Particle Alignment in Photosensitive Polymer Resin: A Preliminary Study for Additive Manufacturing Processes. *Addit. Manuf.* **2018**, *22*, 528−536.
(31) Erb, R. M.; Libanori, R.; Rothfuchs, N.; Studart, A. R. Composites Reinforced in Three Dimensions by Using Low Magnetic Fields. *Science* **2012**, *335*, 199−204.
(32) Martin, J. J.; Fiore, B. E.; Erb, R. M. Designing Bioinspired Composite Reinforcement Architectures via 3D Magnetic Printing. *Nat. Commun.* **2015**, *6*, 8641.
(33) Credi, C.; Fiorese, A.; Tironi, M.; Bernasconi, R.; Magagnin, L.; Levi, M.; Turri, S. 3D Printing of Cantilever-type Microstructures by Stereolithography of Ferromagnetic Photopolymers. *ACS Appl. Mater. Interfaces* **2016**, *8*, 26332−26342.
(34) Lu, L.; Guo, P.; Pan, Y. Magnetic-Field-Assisted Projection Stereolithography for Three-Dimensional Printing of Smart Structures. *J. Manuf. Sci. Eng.* **2017**, *139*, 071008.
(35) Joyee, E. B.; Pan, Y. A Fully Three-Dimensional Printed Inchworm-Inspired Soft Robot with Magnetic Actuation. *Soft Robot* **2019**, *6*, 333−345.
(36) Joyee, E. B.; Pan, Y. Multi-material Additive Manufacturing of Functional Soft Robot. *Procedia Manuf* **2019**, *34*, 566−573.
(37) Joyee, E. B.; Pan, Y. Additive Manufacturing of Multi-material Soft Robot for On-demand Drug Delivery Applications. *J. Manuf. Process* **2020**, *56*, 1178−1184.
(38) Furlani, E. P.; Ng, K. C. Analytical Model of Magnetic Nanoparticle Transport and Capture in the Microvasculature. *Phys. Rev. E: Stat., Nonlinear, Soft Matter Phys.* **2006**, *73*, 061919.
(39) Ghosh, S.; Puri, I. K. Soft Polymer Magnetic Nanocomposites: Microstructure Patterning by Magnetophoretic Transport and Self-assembly. *Soft Matter* **2013**, *9*, 2024−2029.
(40) Timonen, J. V. I.; Latikka, M.; Leibler, L.; Ras, R. H. A.; Ikkala, O. Switchable Static and Dynamic Self-assembly of Magnetic Droplets on Superhydrophobic Surfaces. *Science* **2013**, *341*, 253−257.
(41) Rosensweig, R. E. Magnetic Fluids. *Annu. Rev. Fluid. Mech.* **1987**, *19*, 437−461.
(42) Chung, J. Y.; Nolte, A. J.; Stafford, C. M. Surface Wrinkling: A Versatile Platform for Measuring Thin-film Properties. *Adv. Mater.* **2011**, *23*, 349−368.
(43) Biot, M. A. Bending of an Infinite Beam on an Elastic Foundation. *J. Appl. Math. Mech.* **1922**, *2*, 165−184.
(44) Li, G.; Chen, T.; Yan, B.; Ma, Y.; Zhang, Z.; Yu, T.; Shen, Z.; Chen, H.; Wu, T. Tunable Wettability in Surface-modified ZnO-based Hierarchical Nanostructures. *Appl. Phys. Lett.* **2008**, *92*, 173104.
(45) Young, T. III. An Essay on the Cohesion of Fluids. *Phillos. Trans. R. Soc. London* **1805**, *95*, 65−87.
(46) Cassie, A. B. D.; Baxter, S. Wettability of Porous Surfaces. *Trans. Faraday Soc.* **1944**, *40*, 546−551.
(47) Barbieri, L.; Wagner, E.; Hoffmann, P. Water Wetting Transition Parameters of Perfluorinated Substrates with Periodically Distributed Flat-top Microscale Obstacles. *Langmuir* **2007**, *23*, 1723−1734.
(48) Li, M.; Joung, D.; Hughes, B.; Waldman, S. D.; Kozinski, J. A.; Hwang, D. K. Wrinkling Non-spherical Particles and Its Application in Cell Attachment Promotion. *Sci. Rep.* **2016**, *6*, 30463.
(49) Visaveliya, N. R.; Leishman, C. W.; Ng, K.; Yehya, N.; Tobar, N.; Eisele, D. M.; Köhler, J. M. Surface Wrinkling and Porosity of Polymer Particles Toward Biological and Biomedical Applications. *Adv. Mater. Interfaces* **2017**, *4*, 1700929.
(50) Wang, Z.; Tonderys, D.; Leggett, S. E.; Williams, E. K.; Kiani, M. T.; Spitz Steinberg, R.; Qiu, Y.; Wong, I. Y.; Hurt, R. H. Wrinkled, Wavelength-tunable Graphene-based Surface Topographies for Directing Cell Alignment and Morphology. *Carbon* **2016**, *97*, 14−24.
(51) Guvendiren, M.; Burdick, J. A. The Control of Stem Cell Morphology and Differentiation by Hydrogel Surface Wrinkles. *Biomaterials* **2010**, *31*, 6511−6518.

https://dx.doi.org/10.1021/acsami.0c11693
ACS Appl. Mater. Interfaces 2020, 12, 42357−42368